

## PROTOPLANETARY DISKS IN THE ORION OMC1 REGION IMAGED WITH ALMA

J. A. EISNER<sup>1</sup>, J. M. BALLY<sup>2</sup>, A. GINSBURG<sup>3</sup>, P. D. SHEEHAN<sup>1</sup>*Draft version April 13, 2016*

## ABSTRACT

We present ALMA observations of the Orion Nebula that cover the OMC1 outflow region. Our focus in this paper is on compact emission from protoplanetary disks. We mosaicked a field containing  $\sim 600$  near-IR-identified young stars, around which we can search for sub-mm emission tracing dusty disks. Approximately 100 sources are known proplyds identified with HST. We detect continuum emission at 1 mm wavelengths towards  $\sim 20\%$  of the proplyd sample, and  $\sim 8\%$  of the larger sample of near-IR objects. The noise in our maps allows  $4\sigma$  detection of objects brighter than  $\sim 1.5$  mJy, corresponding to protoplanetary disk masses larger than  $1.5 M_J$  (using standard assumptions about dust opacities and gas-to-dust ratios). None of these disks are detected in contemporaneous CO(2-1) or C<sup>18</sup>O(2-1) observations, suggesting that the gas-to-dust ratios may be substantially smaller than the canonical value of 100. Furthermore, since dust grains may already be sequestered in large bodies in ONC disks, the inferred masses of disk solids may be underestimated. Our results suggest that the distribution of disk masses in this region is compatible with the detection rate of massive planets around M dwarfs, which are the dominant stellar constituent in the ONC.

*Subject headings:* Galaxy:Open Clusters and Associations:Individual: Orion, Stars:Planetary Systems:Protoplanetary Disks, Stars: Pre-Main-Sequence

## 1. INTRODUCTION

Protoplanetary disks are the birth-sites of planetary systems, and the mass distribution of disks relates directly to the masses of planets that may potentially form. The minimum-mass solar nebula (MMSN) needed to form the planets in our Solar System is likely between  $0.01$  and  $0.1 M_\odot$  (e.g., Weidenschilling 1977; Desch 2007). The evolution of disk mass with time provides a separate, but similar constraint. In order to build giant planets on timescales shorter than inferred disk lifetimes, models require disk masses  $\gtrsim 0.01 M_\odot \approx 10 M_J$  (e.g., Hayashi 1981; Alibert et al. 2005). Measuring the distribution and time-evolution of disk mass around young stars provides critical constraints on planet formation.

A widely used method (e.g., Beckwith et al. 1990) for measuring disk masses is to observe emission from optically thin dust, and then use assumed grain properties to convert observed fluxes into dust masses. The assumed opacities imply that most of the dust mass still resides in particles smaller than about 1 mm. If mass is already sequestered in larger bodies like planetesimals (which emit much less per unit mass), then the assumed opacities lead to underestimated disk masses. An assumed gas-to-dust ratio is then used to estimate the total (gas+dust) circumstellar mass. While gas dominates the total mass budget, the mass and surface density of solids are crucial for understanding core formation as well as the potential for accretion of giant planet atmospheres (since fast core formation allows gas accretion before disk dispersal; e.g., Pollack et al. 1996).

At short wavelengths ( $\lambda \lesssim 10 \mu\text{m}$ ), the dust in proto-

planetary disks is optically thick even for masses  $< 10^{-6} M_\odot$ . Observations at sub-mm and mm wavelengths are necessary to measure optically thin dust emission, and hence to determine the total mass of dust in the disk.

While disk masses have been well-studied in low-density star forming regions (e.g., Andrews & Williams 2005, 2007; Andrews et al. 2013; Williams et al. 2013; Carpenter et al. 2014; Ansdell et al. 2015), these are not the typical birth-sites of stars. Most stars form in rich clusters like the Orion Nebula (Lada et al. 1991, 1993; Carpenter 2000; Lada & Lada 2003). Isotopic abundances in our Solar System suggest that it, too, may have formed in a dense, Orion-like environment (e.g., Hester & Desch 2005; Williams & Gaidos 2007). Expanding millimeter continuum surveys to include rich clusters allows the determination of the frequency and evolution of massive disks in typical star (and planet) formation environments.

Rich clusters are relatively challenging to observe because of their distances and high stellar density. High angular resolution and sensitivity are required. Only a handful of rich clusters have been observed to date: the Orion Nebula cluster (Mundy et al. 1995; Bally et al. 1998; Williams et al. 2005; Eisner & Carpenter 2006; Eisner et al. 2008; Mann & Williams 2009, 2010; Mann et al. 2014), IC 348 (Carpenter 2002; Cieza et al. 2015), and NGC 2024 (Eisner & Carpenter 2003; Mann et al. 2015). These existing surveys have detected very few disks with  $\gtrsim 0.01$ – $0.1 M_\odot$  of material, in part because of limited sensitivity and areal coverage. The large number of non-detections implies that the bulk of the disk mass distribution has not yet been constrained. Indeed, stacking analysis of non-detected cluster members suggests average disk masses approximately 10 times smaller than the detection thresholds of previous surveys (e.g., Eisner et al. 2008).

Here we present a new 1.3 mm wavelength interfero-

jeisner@email.arizona.edu

<sup>1</sup> Steward Observatory, University of Arizona, 933 North Cherry Avenue, Tucson, AZ 85721, USA

<sup>2</sup> Department of Astrophysical and Planetary Sciences, University of Colorado, UCB 389, Boulder, CO 80309, USA

<sup>3</sup> ESO Headquarters, Karl-Schwarzschild-Str. 2, 85748 Garching bei Munchen, Germany

metric survey of the Orion Nebula cluster (ONC) with ALMA. The ONC is the logical first choice for early ALMA observations, since it is a young, embedded stellar cluster comprised of hundred of stars spanning a broad mass range. The Trapezium region contains hundreds of stars within a several arcminute radius, and pre-main-sequence evolutionary models (e.g., D’Antona & Mazzitelli 1994) fitted to spectroscopic and/or photometric data indicate that most stars are less than approximately one million years old (e.g., Prosser et al. 1994; Hillenbrand 1997). We can therefore investigate here correlations of disk properties with stellar and/or environmental properties.

## 2. OBSERVATIONS AND DATA REDUCTION

### 2.1. ALMA Cycle 2 Observations

We mapped a region around the OMC1 BN/KL outflow in the Orion Nebula cluster (e.g., Bally et al. 2015a; Snell et al. 1984). The primary goal of the program (as proposed) is to study the outflow in molecular lines, and this will be the topic of a companion paper. Here we focus on the compact circumstellar disks within the imaged region. The map is comprised of 108 mosaicked pointings in the northwest region of the OMC1 outflow and 39 pointings in the southeast region. The fields were observed at 230 GHz frequency (Band 6), corresponding to a wavelength of 1.3 mm. Observations were taken between 19 July 2014 and 05 April 2015.

The angular resolution of the observations was approximately  $1''$ . At the distance to Orion,  $\sim 400$  pc (e.g., Sandstrom et al. 2007; Menten et al. 2007; Kraus et al. 2007), the linear resolution is approximately 400 AU. Thus, any objects with radii smaller than  $\sim 200$  AU will be unresolved by these observations. ALMA Compact Array (ACA) observations were also obtained as part of this program in order to map the extended outflow well, but we do not use these data here since our focus is on the compact disks.

We observed continuum emission using four 1.875 GHz- wide bands centered at 216, 228, 231, and 233 GHz. Substantial parts of the bandpass contained spectral line emission and were flagged for the continuum data reduction. Averaging continuum data over all spectral windows, the effective central frequency is 225 GHz.

One 2 GHz window was devoted to CO(2-1) at 231 GHz, and two other windows targeted C<sup>18</sup>O and SiO at 218 GHz, and SO at 216 GHz. All spectral windows had frequency resolution of about 1 MHz, providing velocity resolution of 1.3 km s<sup>-1</sup>.

We adopted the reduced ALMA data products. The reduction included heavy flagging to remove strong spectral lines from the continuum, as well as the standard flux, bandpass, and gain calibrations. The sources used for calibration included J0607-0834, J0541-0541, J0423-013, J0725-0054, Uranus, and Ganymede. The *uv* data were inverted using a Briggs robust weighting parameter of 0.5, resulting in a synthesized beam with dimensions  $\sim 1''.4 \times 0''.8$ . The rms varies across the field because of strong extended emission from OMC1. Typical noise values in clean regions of the continuum image are 0.5 mJy/beam. The noise is 5 mJy km s<sup>-1</sup> in a typical spectral line channel, although in channels with strong emission from the OMC1 outflow the rms can rise to  $\sim 20$

TABLE 1  
NEW NEAR-IR SOURCES DETECTED IN  
GEMS IMAGING

ID	$\alpha$ (J2000)	$\delta$ (J2000)	$m_K$
GeMS 1	5 35 12.95	-5 22 44.34	14.0
GeMS 2	5 35 12.35	-5 22 41.35	14.2
GeMS 3	5 35 15.39	-5 22 39.93	14.0
GeMS 4	5 35 13.30	-5 22 39.32	13.9
GeMS 5	5 35 14.50	-5 22 38.78	14.1
GeMS 6	5 35 12.31	-5 22 34.19	14.4
GeMS 7	5 35 15.56	-5 22 20.13	13.4
GeMS 8	5 35 14.20	-5 22 12.99	13.1
GeMS 9	5 35 13.57	-5 22 9.65	13.8
GeMS 10	5 35 10.58	-5 21 14.08	13.6
GeMS 11	5 35 12.08	-5 21 12.95	14.0
GeMS 12	5 35 13.62	-5 21 5.22	13.0
GeMS 13	5 35 15.37	-5 20 47.37	14.2
GeMS 14	5 35 13.09	-5 20 45.92	14.0
GeMS 15	5 35 11.87	-5 20 43.51	11.8
GeMS 16	5 35 12.62	-5 20 43.07	9.2
GeMS 17	5 35 14.65	-5 20 42.70	7.2
GeMS 18	5 35 13.27	-5 20 41.99	12.7
GeMS 19	5 35 15.85	-5 20 40.34	8.9
GeMS 20	5 35 12.11	-5 20 39.95	10.6
GeMS 21	5 35 13.60	-5 20 39.30	9.1
GeMS 22	5 35 12.81	-5 20 39.16	11.0
GeMS 23	5 35 12.81	-5 20 35.10	8.8
GeMS 24	5 35 12.00	-5 20 33.40	7.5
GeMS 25	5 35 13.61	-5 20 31.51	8.5
GeMS 26	5 35 13.07	-5 20 30.42	8.0
GeMS 27	5 35 15.27	-5 20 28.99	9.6
GeMS 28	5 35 14.76	-5 20 28.99	7.7
GeMS 29	5 35 12.23	-5 20 26.52	12.5
GeMS 30	5 35 14.17	-5 20 23.65	9.1
GeMS 31	5 35 10.50	-5 20 21.03	13.8
GeMS 32	5 35 13.33	-5 20 19.09	8.6
GeMS 33	5 35 14.70	-5 20 17.13	11.5
GeMS 34	5 35 15.19	-5 20 15.01	9.7
GeMS 35	5 35 10.98	-5 20 12.94	13.7
GeMS 36	5 35 14.17	-5 20 8.17	11.8
GeMS 37	5 35 14.21	-5 20 4.50	7.9
GeMS 38	5 35 14.25	-5 20 3.84	11.8
GeMS 39	5 35 11.90	-5 20 2.42	9.4
GeMS 40	5 35 14.84	-5 20 2.29	14.4

mJy km s<sup>-1</sup>.

### 2.2. GeMS Near-IR Imaging

We searched for sub-mm emission toward the positions of known near-IR sources, because detection of sub-mm continuum flux would indicate disks (as opposed to embedded spherical sources; e.g., Beckwith et al. 1990). We therefore make use of previous near-IR observations that identified cluster members (Hillenbrand & Carpenter 2000). We supplement this catalog with new data, because the previous observations did not cover the complete region we mapped with ALMA. We observed the OMC1 region in Orion with GeMS at the Gemini South telescope between 30 December 2012 and 28 February 2013 (see Bally et al. 2015a). We observed in the  $K_s$  filter, as well as narrow Fe[II] and H<sub>2</sub> filters, producing images with angular resolutions of  $\sim 0''.06$ . The  $K_s$  image is shown in Figure 1.

We used the IDL implementation of the *find* algorithm to identify stellar sources in the  $K_s$ -band image. We cross-referenced these with the Hillenbrand & Carpenter (2000) catalog, and kept only previously un-identified objects. We also visually inspected all sources, and discarded several spurious detections in the bright central

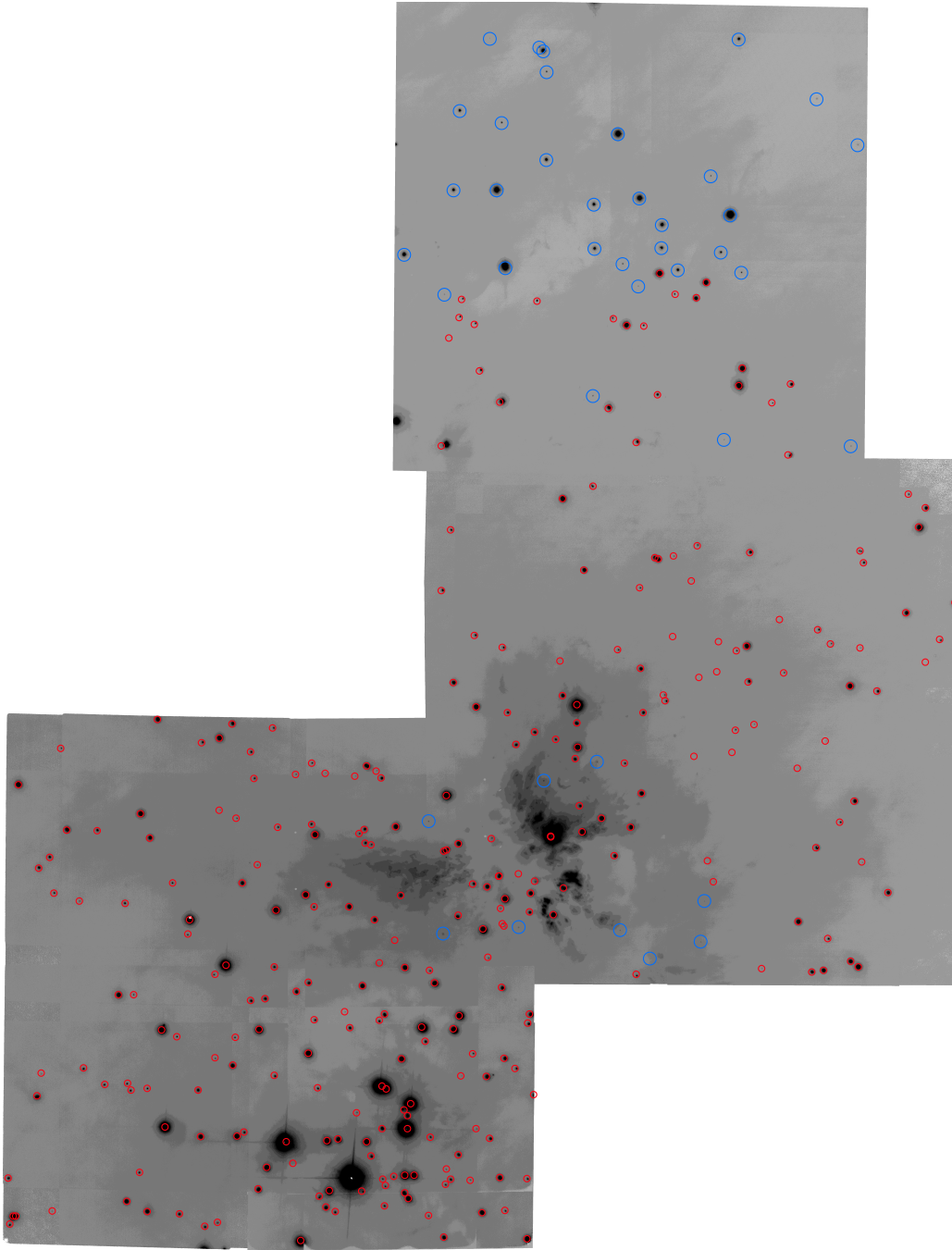


FIG. 1.— Mosaicked image of the OMC1 region in the  $K_s$  filter, obtained with GeMS. The positions of previously-known near-IR cluster members (Hillenbrand & Carpenter 2000) are indicated with small red circles. We detected an additional 40 stars in the image, indicated with blue circles. Some of these were outside the area covered by the survey of Hillenbrand & Carpenter (2000), while others can be distinguished in crowded regions because of the higher angular resolution of our observations.

regions of the OMC1 outflow. 40 new detections remain after this process. We performed aperture photometry for these sources, and used previous measurements of Hillenbrand & Carpenter (2000) for stars in our field to calibrate the flux scale. Source positions and magnitudes are listed in Table 1.

Without proper motions, the cluster membership of these newly identified sources is uncertain. However all objects are also detected in narrowband filters tuned to Fe[II] in the  $H$ -band and  $H_2$  in the  $K$ -band. Comparison of the color-magnitude relations of new detections

and previously cataloged sources in Hillenbrand & Carpenter (2000) suggest that they trace the same stellar population. This suggests that contamination by background or foreground objects, while possible, is likely no worse than in the sample from Hillenbrand & Carpenter (2000).

### 3. RESULTS

We searched for 1.3 mm continuum emission towards the positions of HST-detected proplyds (Ricci et al. 2008) and near-IR detected sources (Hillenbrand & Carpenter

TABLE 2  
FLUXES AND INFERRED DISK MASSES FOR ALMA-DETECTED SOURCES

ID	$\alpha$ (J2000)	$\delta$ (J2000)	$M_*$ ( $M_\odot$ )	$F_{\lambda 1.3\text{mm}}$ (mJy)	$F_{\text{dust}}$ (mJy)	$M_{\text{disk}}$ ( $M_{\text{Jup}}$ )
HC455	5 35 8.93	-5 22 30.00	0.2	$1.3 \pm 0.2$	$1.3 \pm 0.2$	$1.6 \pm 0.2$
HC592	5 35 9.35	-5 21 41.60	—	$5.3 \pm 0.4$	$5.3 \pm 0.4$	$6.5 \pm 0.5$
HC588	5 35 9.93	-5 21 43.40	—	$2.3 \pm 0.3$	$2.3 \pm 0.3$	$2.8 \pm 0.4$
102-233	5 35 10.13	-5 22 32.74	0.5	$2.0 \pm 0.4$	$2.0 \pm 0.4$	$2.5 \pm 0.5$
102-021	5 35 10.19	-5 20 20.99	—	$5.4 \pm 0.5$	$5.4 \pm 0.5$	$6.7 \pm 0.6$
HC647	5 35 10.32	-5 21 13.10	0.3	$16.3 \pm 1.3$	$16.3 \pm 1.3$	$20.1 \pm 1.6$
HC374	5 35 10.39	-5 22 59.80	—	$12.3 \pm 1.1$	$12.3 \pm 1.1$	$15.2 \pm 1.4$
HC421	5 35 10.58	-5 22 44.80	0.3	$2.1 \pm 0.4$	$2.1 \pm 0.4$	$2.6 \pm 0.5$
106-156	5 35 10.58	-5 21 56.24	—	$18.6 \pm 1.5$	$18.6 \pm 1.5$	$23.0 \pm 1.9$
HC582	5 35 10.97	-5 21 46.40	—	$6.3 \pm 0.7$	$6.3 \pm 0.7$	$7.8 \pm 0.9$
HC415	5 35 11.04	-5 22 46.70	—	$9.8 \pm 0.9$	$9.8 \pm 0.9$	$12.1 \pm 1.1$
HC750	5 35 11.42	-5 21 44.60	—	$5.6 \pm 0.6$	$5.6 \pm 0.6$	$6.9 \pm 0.7$
HC611	5 35 11.77	-5 21 32.80	—	$2.7 \pm 0.4$	$2.7 \pm 0.4$	$3.3 \pm 0.5$
HC573	5 35 11.81	-5 21 49.30	—	$3.0 \pm 0.7$	$0.0 \pm 0.9$	$0.0 \pm 1.1$
HC672	5 35 11.86	-5 21 0.30	—	$9.3 \pm 0.8$	$9.3 \pm 0.8$	$11.5 \pm 1.0$
124-132	5 35 12.38	-5 21 31.39	—	$2.8 \pm 0.6$	$2.8 \pm 0.6$	$3.5 \pm 0.7$
GEMS23	5 35 12.81	-5 20 35.10	—	$1.8 \pm 0.3$	$1.8 \pm 0.3$	$2.2 \pm 0.4$
HC606	5 35 12.85	-5 21 33.90	—	$10.7 \pm 1.3$	$10.7 \pm 1.3$	$13.2 \pm 1.6$
HC608	5 35 12.89	-5 21 33.70	—	$8.3 \pm 1.3$	$8.3 \pm 1.3$	$10.2 \pm 1.6$
131-046	5 35 13.05	-5 20 45.79	—	$1.8 \pm 0.3$	$1.8 \pm 0.3$	$2.2 \pm 0.4$
HC682	5 35 13.22	-5 20 52.80	0.5	$4.2 \pm 0.4$	$4.2 \pm 0.4$	$5.2 \pm 0.5$
132-042	5 35 13.24	-5 20 41.94	—	$1.5 \pm 0.4$	$1.5 \pm 0.4$	$1.9 \pm 0.5$
HC602	5 35 13.73	-5 21 35.90	—	$4.9 \pm 1.0$	$4.9 \pm 1.0$	$6.1 \pm 1.2$
138-207	5 35 13.78	-5 22 7.39	—	$25.8 \pm 6.8$	$25.8 \pm 6.8$	$31.9 \pm 8.4$
GEMS37	5 35 14.21	-5 20 4.50	—	$2.0 \pm 0.4$	$2.0 \pm 0.4$	$2.5 \pm 0.5$
GEMS38	5 35 14.25	-5 20 3.84	—	$1.8 \pm 0.4$	$1.8 \pm 0.4$	$2.2 \pm 0.5$
HC657	5 35 14.72	-5 21 6.30	—	$9.3 \pm 1.0$	$9.3 \pm 1.0$	$11.5 \pm 1.2$
GEMS28	5 35 14.76	-5 20 28.99	—	$12.0 \pm 1.2$	$12.0 \pm 1.2$	$14.8 \pm 1.5$
158-327	5 35 15.79	-5 23 26.51	3.0	$17.3 \pm 2.8$	$5.0 \pm 2.8$	$6.2 \pm 3.5$
158-323	5 35 15.83	-5 23 22.59	0.8	$11.8 \pm 2.8$	$2.0 \pm 2.8$	$2.5 \pm 3.5$
HC342	5 35 15.85	-5 23 11.00	5.0	$6.5 \pm 1.2$	$6.5 \pm 1.2$	$8.0 \pm 1.5$
HC370	5 35 15.88	-5 23 2.00	—	$3.9 \pm 0.9$	$4.0 \pm 1.3$	$5.0 \pm 1.7$
163-317	5 35 16.27	-5 23 16.51	—	$12.1 \pm 1.8$	$2.0 \pm 1.9$	$2.5 \pm 2.3$
167-317	5 35 16.74	-5 23 16.51	3.0	$21.2 \pm 2.3$	$3.0 \pm 2.3$	$3.7 \pm 2.8$
168-326	5 35 16.83	-5 23 25.91	—	$17.1 \pm 2.4$	$4.0 \pm 2.4$	$5.0 \pm 3.0$
170-301	5 35 16.95	-5 23 0.91	—	$3.6 \pm 0.7$	$3.0 \pm 0.9$	$3.7 \pm 1.1$
170-249	5 35 16.96	-5 22 48.51	0.4	$12.0 \pm 1.4$	$9.0 \pm 2.1$	$11.1 \pm 2.5$
173-236	5 35 17.34	-5 22 35.81	3.0	$13.6 \pm 1.4$	$12.0 \pm 2.1$	$14.8 \pm 2.5$
HC422	5 35 17.38	-5 22 45.80	—	$3.1 \pm 0.7$	$3.1 \pm 0.7$	$3.8 \pm 0.9$
175-251	5 35 17.47	-5 22 51.26	0.3	$2.9 \pm 0.7$	$3.0 \pm 1.2$	$3.7 \pm 1.5$
178-258	5 35 17.84	-5 22 58.15	0.2	$5.2 \pm 0.7$	$5.2 \pm 0.7$	$6.4 \pm 0.9$
181-247	5 35 18.08	-5 22 47.10	—	$3.1 \pm 0.6$	$5.0 \pm 0.8$	$6.2 \pm 1.0$
HC436	5 35 18.38	-5 22 37.50	0.7	$3.6 \pm 0.5$	$0.0 \pm 0.5$	$0.0 \pm 0.6$
HC482	5 35 18.85	-5 22 23.10	0.2	$8.3 \pm 0.8$	$8.3 \pm 0.8$	$10.2 \pm 1.0$
HC351	5 35 19.07	-5 23 7.50	—	$5.6 \pm 0.6$	$5.6 \pm 0.6$	$6.9 \pm 0.7$
191-232	5 35 19.13	-5 22 31.20	—	$1.8 \pm 0.4$	$1.8 \pm 0.4$	$2.2 \pm 0.5$
HC366	5 35 19.63	-5 23 3.60	0.1	$4.0 \pm 0.5$	$4.0 \pm 0.5$	$4.9 \pm 0.6$
198-222	5 35 19.82	-5 22 21.55	—	$4.6 \pm 0.6$	$4.0 \pm 0.8$	$5.0 \pm 1.0$
202-228	5 35 20.15	-5 22 28.30	—	$5.4 \pm 0.7$	$5.4 \pm 0.7$	$6.7 \pm 0.9$

NOTE. — Stellar masses, where available, are taken from the literature (Hillenbrand 1997; Luhman et al. 2000; Slesnick et al. 2004; Hillenbrand et al. 2013; Ingraham et al. 2014).

2000)<sup>4</sup>. We employed a detection threshold of  $4\sigma$  above the locally-determined noise level for each optical/near-IR source. This threshold ensures that  $\ll 1$  detection is expected from noise fluctuations across the entire sample of known cluster members (we do expect  $> 1$  noise spike above the  $3\sigma$  level).

Including the newly detected sources in our GeMS imaging, our ALMA maps included 593 near-IR targets. Approximately 100 of these objects are also classified as proplyds based on HST imaging. We detected ALMA emission towards 21 of the known proplyds, a detection rate of  $\sim 20\%$ . The detection rate among the larger sample of near-IR targets was somewhat lower,  $\sim 8\%$ , with

<sup>4</sup> Most of the proplyds are also detected as near-IR objects.

ALMA emission seen toward 47 objects (2 proplyds in our sample are not included in the near-IR sample).

Some targets are found in regions of the ONC with bright background emission due to nearby sources or dense regions of the molecular cloud. We corrected the measured fluxes by subtracting the background emission measured in annuli around each target. This background level is less than 10% of the target fluxes in all cases, so represents only a minor correction.

In total, ALMA emission above the  $4\sigma$  level was seen towards 49 cluster members (Table 2; Figure 2). Of these, 11 were detected in previous, less sensitive observations at a similar wavelength (Eisner et al. 2008). Five of this sub-sample were also detected in Cycle 0 ALMA observations at  $860 \mu\text{m}$  (Mann et al. 2014), and three



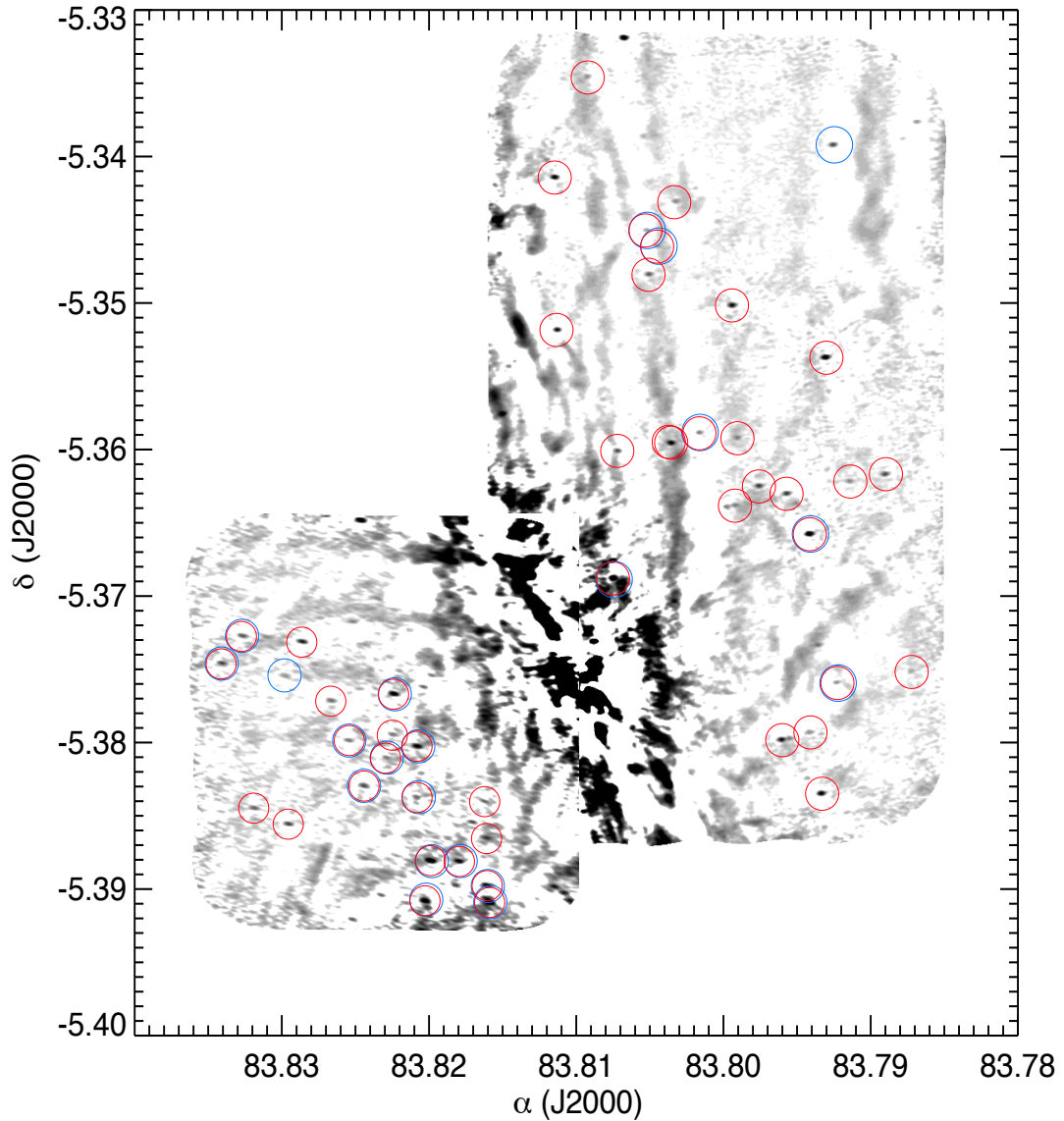


FIG. 2.— Mosaicked image of the OMC1 region in  $\lambda 1.3$  mm continuum emission, obtained with ALMA. Known near-IR sources detected above  $4\sigma$  are shown with red circles. Blue circles indicate emission detected above  $4\sigma$  towards known HST-imaged proplyds from Ricci et al. (2008). All but two of the proplyds in this field have known near-IR counterparts.

were detected previously at  $\lambda 3$ mm (Eisner & Carpenter 2006; Mundy et al. 1995). We thus detected millimeter-wavelength emission for the first time towards 38 stars in the ONC.

Given the strong ionization field near the Trapezium stars, gas in circumstellar disks or outflows can emit free-free emission. Contributions of millimeter-wavelength free-free emission must be accounted for in order to correctly determine the flux arising from dusty disk matter. The spectrum of optically thin free-free emission is relatively flat compared to that of dust emission, and so observations at cm wavelengths can be used to constrain free-free emission (e.g., Eisner et al. 2008).

We used previous observations of the ONC at cm wavelengths from Felli et al. (1993a,b); Zapata et al. (2004); Forbrich et al. (2007) to search for free-free emission from our sample. Nine of the sources detected in our ALMA observations are also seen in these previous observations. However previous surveys only constrained free-

free emission at the  $\sim 1$  mJy level for most of our targets. Given the roughly flat spectrum of optically thin free-free emission, these measurements can only constrain contributions at ALMA wavelengths at approximately the same level. Since our ALMA observations are sensitive to emission at  $< 1$  mJy, we need deeper cm-wavelength observations to constrain the free-free emission well for our sample.

Sheehan et al. (2016) conducted a new survey of the ONC with the JVLA, reaching sensitivities of  $\lesssim 30 \mu\text{Jy}$  at cm wavelengths. Their maps of 3.6 and 6 cm continuum emission cover the entire area of the ALMA mosaic presented here. In addition to the 9 targets with cm emission noted above, the deeper cm-wavelength data reveal free-free emission from five other sources in our sample. The 14 objects with cm-wavelength detections are shown in Figure 3.

For these sources, we constructed a model that includes optically thick free-free emission past a turnover

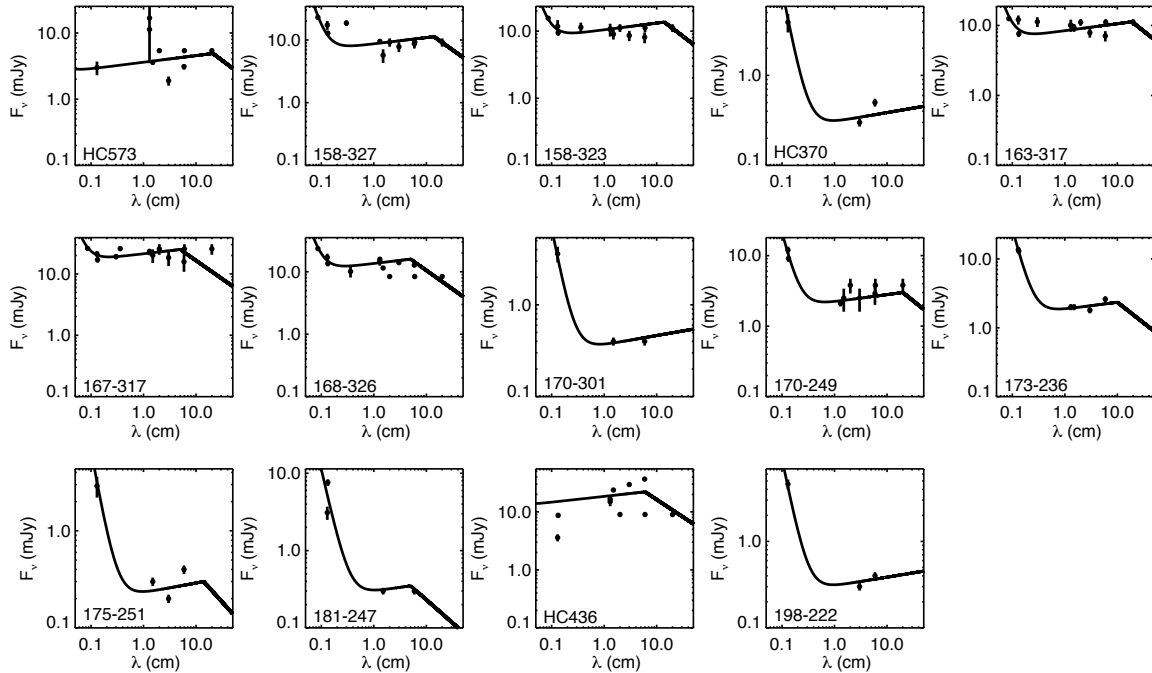


FIG. 3.— Long-wavelength fluxes of sources detected in our ALMA observations that are also detected at cm wavelengths. The solid curves shows models, including optically thin and thick free-free emission and optically thin dust emission, fitted to the data for each object.

wavelength, thin free-free emission short-ward of that turnover, and optically-thin dust with  $\beta = 1$  (as in Eisner et al. 2008). Free parameters in the model are the turnover wavelength of free-free emission, and the free-free and dust fluxes at the observed ALMA wavelength. Best-fit models are shown in Figure 3. Estimated free-free and dust contributions to the flux at the observed ALMA wavelength are listed in Table 2.

The remaining objects detected in our ALMA mosaic are not seen in cm-wavelength observations. These non-detections imply that the cm-wavelength flux, and hence the potential free-free contribution at mm wavelengths, is  $\lesssim 0.03$  mJy for these sources. Since the observed ALMA fluxes are all  $\geq 1.3$  mJy, we can be confident that we have detected dust emission. The  $\lesssim 0.03$  mJy uncertainties resulting from potential low-level free-free emission are much smaller than the uncertainties in the mm-wavelength flux measurements.

Continuum fluxes (less free-free contributions) are converted to disk dust masses under the simple assumption of optically thin dust:

$$M_{\text{dust}} = \frac{S_{\nu, \text{dust}} d^2}{\kappa_{\nu, \text{dust}} B_{\nu}(T_{\text{dust}})}. \quad (1)$$

Here,  $\nu$  is the observed frequency,  $S_{\nu, \text{dust}}$  is the observed flux due to cool dust,  $d$  is the distance to the source,  $\kappa_{\nu, \text{dust}} = \kappa_0(\nu/\nu_0)^\beta$  is the dust mass opacity,  $T_{\text{dust}}$  is the dust temperature, and  $B_{\nu}$  is the Planck function. We assume  $d \approx 400$  pc,  $\kappa_0 = 2$  cm<sup>2</sup> g<sup>-1</sup> at 1.3 mm,  $\beta = 1.0$  (Hildebrand 1983; Beckwith et al. 1990), and  $T_{\text{dust}} = 20$  K (based on the average dust temperature inferred for Taurus; Andrews & Williams 2005; see also the discussion in Carpenter 2002; Williams et al. 2005). The dust mass can be converted into a total circumstellar mass by assuming the canonical gas-to-dust mass ratio of

100. For easy comparison with the MMSN, we use these total disk masses in the figures and in Table 2. However we discuss potential deviations from this assumed gas-to-dust ratio, and the implications, in §4.5.

No sources are detected above the  $4\sigma$  level in CO(2-1) emission. The  $4\sigma$  noise level in the line-integrated map is 17 mJy km s<sup>-1</sup>. Indeed, for the sample of continuum detections, where a  $3\sigma$  threshold of 12 mJy km s<sup>-1</sup> can be employed with minimal risk of false positives, we still detect no line emission from any sources (Figure 4). As expected, no sources are detected in C<sup>18</sup>O emission either.

## 4. DISCUSSION

### 4.1. Disk Detection Rates

The detection rate among near-IR-selected sources that lie within the ALMA mosaic is  $\sim 8\%$ , lower than the detection rate of  $\sim 20\%$  for HST-identified proplyds (all but two of which are also included in the near-IR selected sample). This discrepancy may reflect a selection bias caused by strong free-free emission in proplyds that lead to easier detection at mm wavelengths (despite a low intrinsic dust disk mass). Among our sample, 7 proplyds have strong contributions from free-free emission to the observed mm-wavelength flux. In contrast, only two near-IR-selected targets (that are not also identified as proplyds) are strongly affected by free-free emission. Assuming these objects would not have been detected if not for their strong free-free emission, the discrepancy in detection rates becomes smaller.

However some difference remains, perhaps because the near-IR sample is more likely to include some disk-less stars, or foreground or background objects. Given the selection of proplyds based on their morphologies and observed emission from ionized gas, their status as cluster members is indeed easier to determine.

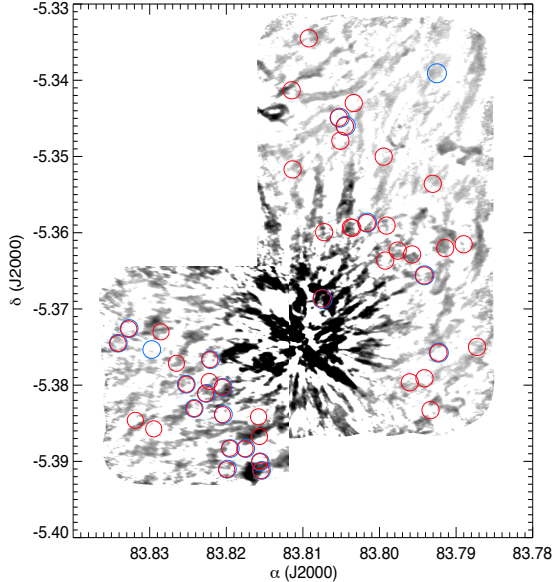


FIG. 4.— ALMA image of the OMC1 region in line-integrated CO(2-1) emission. The locations of disks detected in continuum emission are indicated with circles, as in Figure 2. We see no compact CO emission towards any of these objects.

#### 4.2. Disk Mass Distribution

The distribution of disk masses is plotted as a histogram in Figure 5. The vast majority of detections have dust disk masses  $\lesssim 0.03 M_J$  (or total gas+dust masses  $\lesssim 3 M_J$  assuming a gas-to-dust ratio of 100). The noise in the maps means that less massive disks would probably have been undetected. Given that most cluster members were not detected in our observations, we infer that the peak of the disk dust mass distribution likely lies at masses smaller than  $0.03 M_J$ .

There are a number of objects with inferred dust+gas disk masses  $\gtrsim 0.01 M_\odot$ . From Table 2, we see that 12 sources have disk masses above this level, representing  $\sim 25\%$  of all detections, and  $\sim 2\%$  of all cluster members surveyed.

#### 4.3. Disk Mass versus Cluster Radius

The intense photoionizing radiation of  $\theta^1$  Ori C and other Trapezium stars can lead to photoevaporation of disks in the ONC (e.g., Johnstone et al. 1998; Scally & Clarke 2001). One might therefore expect to see some dependence of disk mass on cluster radius, since disks in the cluster outskirts would be less affected by photoionizing radiation.

Intriguingly, the inner disk fraction may decrease at larger cluster radii (Hillenbrand et al. 1998), contrary to this expectation. Recent work shows no evidence for a decrease in inner disk fraction near to O stars in the ONC or other regions (Richert et al. 2015). However inner disks are tightly bound to their central stars and may be less affected by photoevaporation than outer disks.

At mm/sub-mm wavelengths, where observations are sensitive to large, massive disks, previous observations suggested a truncated disk mass distribution within  $0.03$  pc of  $\theta^1$  Ori C, whereas a broader distribution exists at larger cluster radii (Mann et al. 2014). This dichotomy was interpreted as evidence that stars within the EUV-dominated region of the Trapezium stars experience sig-

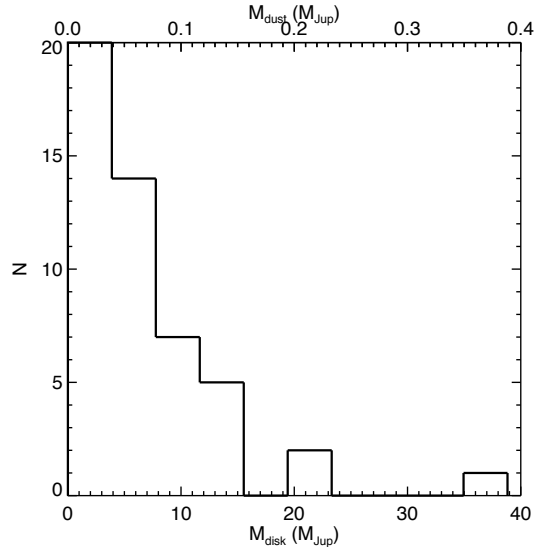


FIG. 5.— Disk mass distribution for the sources detected with ALMA. We label the mass of disk dust (top axis) as well as the gas+dust mass (bottom axis); the latter assumes a gas-to-dust ratio of 100.

nificant disk evaporation, while disks can survive intact in the FUV-dominated region at larger cluster radii.

Kinematics suggest that the stellar population is unrelaxed, and younger than the crossing time for the entire cluster (e.g., Tobin et al. 2009). However, the crossing time within a fraction of a parsec is substantially shorter than the age of the region. It is therefore unclear whether stars that currently lie within  $0.03$  pc of  $\theta^1$  Ori C have been there for a substantial fraction of the lifetime of the cluster. On the other hand, it may be that the ionization front from  $\theta^1$  Ori C has turned on recently, uncovering proplyds as it advances through the cloud.

Our observations support the conclusion of Mann et al. (2014). As seen in Figure 6, disk masses within about  $0.03$  pc range from  $0$  to  $< 10 M_J$ , while the range extends to  $> 30 M_J$  at larger distances. This result is not statistically significant based on our dataset. The Fisher exact test suggests that there is a 9% probability that a single disk mass distribution applies within  $0.03$  pc and at larger radial distances.

If we include the ALMA data of Mann et al. (2014), which are sensitive to the same range of disk masses probed in this work, we can improve the significance of this result. Using both datasets, the Fisher exact test gives only a 0.7% probability of a single distribution, suggesting a difference between the disk population within and beyond  $\sim 0.03$  pc of  $\theta^1$  Ori C significant at  $\sim 3\sigma$ . Even if we exclude the two very massive disks in Mann et al. (2014) at  $\gtrsim 1$  pc distance, the probability of a single distribution is still only  $\sim 1\%$ .

#### 4.4. Disk Mass versus Stellar Mass

Previous investigations of near-IR excess emission showed the inner disk fraction for stars in Orion to be largely independent of stellar age and mass, although there are indications of a paucity of disks around very massive stars (Hillenbrand et al. 1998; Lada et al. 2000). However this correlation has not been studied in the ONC for massive disks as traced by mm/sub-mm emission.

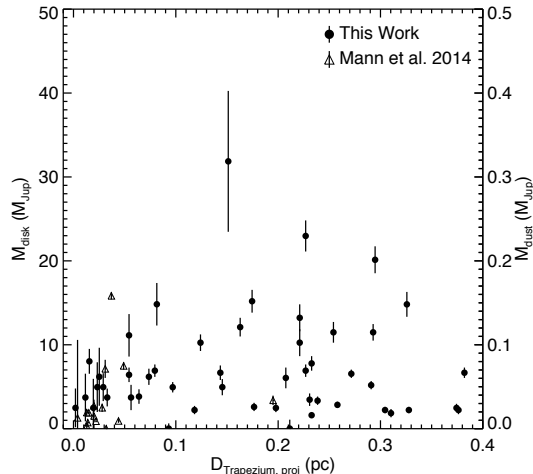


FIG. 6.— Disk mass versus projected separation from the Trapezium stars, for the sources detected with ALMA. Our measurements are plotted with filled circles. We also include the measured disk masses for additional sources from Mann et al. (2014), plotting them as open triangles. Two massive disks detected at  $> 1$  pc distance by Mann et al. (2014) are excluded from this plot.

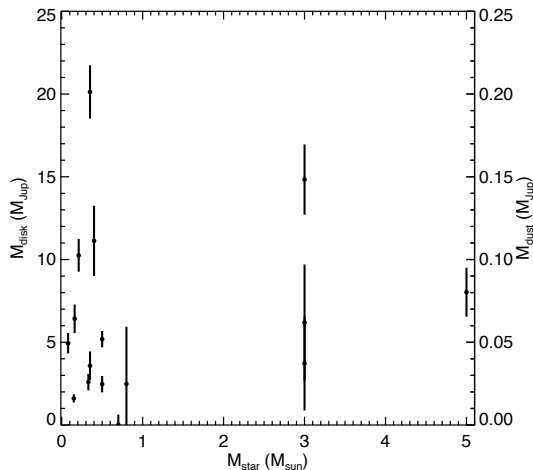


FIG. 7.— Disk mass versus stellar mass for the subset of our sample with spectroscopically-determined stellar masses.

Observations of Taurus suggest a significant correlation between disk and stellar mass (Andrews et al. 2013). While we see no such correlation in the ONC, at present the statistical significance of this result is limited both by the small number of ALMA detections and the small number of spectroscopically-determined stellar masses for extincted cluster members. To date, stellar masses have been determined spectroscopically for less than half of the sources in our ALMA-detected sample (Hillenbrand 1997; Luhman et al. 2000; Slesnick et al. 2004; Hillenbrand et al. 2013; Ingraham et al. 2014). We plot disk mass versus stellar mass for this sub-sample in Figure 7. In the near future, deeper ALMA observations will yield a larger sample of disk masses, and near-IR spectroscopy will provide stellar masses of embedded cluster members in the ONC.

#### 4.5. Gas-to-Dust Ratios

While we determined dust masses above, and converted them to total gas+dust masses using an assumed

gas-to-dust ratio, one can also use spectral line data to attempt to measure gas masses directly (e.g., Williams & Best 2014; Miotello et al. 2014). Models presented in Williams & Best (2014) suggest that a disk with total mass of  $0.01 M_{\odot}$  should exhibit a  $^{12}\text{CO}(2-1)$  flux of  $\sim 0.1\text{--}5 \text{ Jy km s}^{-1}$ . While this spans a wide range (indeed, Williams & Best 2014; Miotello et al. 2014, suggest using line ratios for more accurate gas mass estimates), even the lower limit is higher than the detection threshold in our line maps,  $\sim 12 \text{ mJy km s}^{-1}$ . Thus, we would expect that most disks in our sample detected in 1.3 mm continuum emission with ALMA should be detected in CO.

The models in Williams & Best (2014) included a range of disk sizes, with radii as small as 30 AU. Since  $^{12}\text{CO}(2-1)$  is generally optically thick, still smaller disks—at fixed mass—might produce lower flux. However, inferred sizes of proplyds are typically larger than the lower limit in Williams & Best (2014). The mean disk radius for a sample of 134 proplyds observed with *HST* is 35 AU (Vicente & Alves 2005). Many proplyds, including some within 0.03 pc of  $\theta^1\text{Ori C}$ , have radii greater than 100 AU (Vicente & Alves 2005; Eisner et al. 2008). Thus it seems unlikely that the lack of CO detections can be explained by unusually compact disks.

The non-detection of any disk in the CO data suggests a relative lack of gas in these disks. The gas-to-dust ratio is likely much smaller than 100. This is consistent with previous results: Williams & Best (2014) inferred values of the gas-to-dust ratio of  $\lesssim 20$  in Taurus. In the ONC, where strong ionization from  $\theta^1\text{C}$  and the other Trapezium stars can cause strong photoevaporative winds from circumstellar disks, we expect still lower gas-to-dust ratios (e.g., Throop & Bally 2005).

Detecting gas from disks in the ONC likely requires better sensitivity than the observations presented here. Assuming a gas-to-dust ratio of 10, the distribution of  $M_{\text{dust}}$  values shown in Figure 5 suggests that we would need sufficient sensitivity to detect  $\lesssim 1 M_J$  of gas. Using the lower limit from Williams & Best (2014), this could represent  $\text{CO}(2-1)$  flux  $\lesssim 10 \text{ mJy km s}^{-1}$ .

One caveat is that the strong molecular emission from the Orion cloud could obscure gas emission from disks lying in the background. While most proplyds appear to reside in front of the cloud, it is possible that some gas-rich disks in the background could be missed.

There are strong detections of a few large proplyds at relatively large cluster radii (e.g., Williams et al. 2014; Bally et al. 2015b). Such large, gas-rich disks would be more likely to photoevaporate if they resided close to the Trapezium stars. Thus, the gas content of many, if not most, disks in the ONC, may be substantially lower than these examples.

#### 4.6. Implications for Giant Planet Formation

The disk mass distribution shown in Figure 5 indicates that only a small percentage of ONC cluster members have masses comparable to or larger than the MMSN. Adopting  $10 M_J$  as the minimum value of the MMSN (Weidenschilling 1977), we find 12 disks above this level. Compared to the  $\sim 600$  near-IR and optically identified cluster members surveyed, this represents a detection rate of only 2%.

Such a low detection rate may be at odds with the known existence of giant planets around other stars (e.g., Wright et al. 2011). Around FGK stars, the detection rate of planets more massive than Jupiter is  $\sim 10\%$ , and extrapolation to larger orbital radii suggests that up to 20% of FGK stars in the Galaxy may host giant planets (Cumming et al. 2008). The detection rate around M dwarfs is  $\sim 5$ –10 times lower<sup>5</sup>,  $\sim 2\%$  (Cumming et al. 2008; Johnson et al. 2010). The distribution of stellar masses in the ONC peaks at  $0.2 M_{\odot}$  (Hillenbrand 1997; Slesnick et al. 2004), implying most cluster members are M dwarfs.

A giant planet detection rate near 2% may therefore be an appropriate benchmark in this case. Since  $\sim 2\%$  of ONC cluster members in our survey have disk masses similar to the MMSN, the planet formation potential in this young region seems close to the final outcomes seen around main-sequence M dwarfs in the field.

However the disk masses plotted in Figure 5 assume a gas-to-dust ratio of 100. The non-detection of any sources in CO emission (as well as previous results for young stars in Taurus; Williams & Best 2014) suggests that this ratio may be substantially lower. In that case, the fraction of disks with total masses greater than  $10 M_J$  could approach zero.

According to the approach used to derive the MMSN, this would imply that none of the systems in the ONC can form Jupiter-mass planets. However this conclusion can be avoided if we re-examine a key assumption in the MMSN model. Specifically, that model assumes that all of the heavy elements in Jupiter and other planets had to condense out from Solar-composition gas. If there is sufficient dust to build planetary cores (perhaps from an earlier condensation event), then a much smaller amount of gas is needed to build the planetary atmospheres. For example, a  $30 M_{\oplus}$  solid core, massive enough to accrete a large gaseous atmosphere (e.g., Pollack et al. 1996), requires only  $\sim 1 M_J$  of solar-composition gas to become a Jupiter-like planet.

It is the mass of disk solids, which determine the formation timescale of a crossover-mass core, that provides a tighter constraint on planet-formation potential. A more accurate definition for the minimum mass of dust and gas needed to form a planetary system like ours may be  $> 0.1 M_J$  of dust and  $> 1 M_J$  of gas. This argument suggests that 2% is the correct number for gauging giant planet formation potential, since a gas+dust mass of  $10 M_J$  in Figure 5 corresponds to  $0.1 M_J$  of dust.

Accounting for uncertain dust opacity (i.e., mass hidden in already-grown pebbles or planetesimals), the solid content of disks in the ONC may be still higher than inferred above. Lower dust opacities, which account for this hidden mass of solids, are physically plausible as long as they do not push the high end of the inferred disk mass distribution into a gravitationally unstable regime. Assuming most stars in our sample have masses  $\lesssim 1 M_{\odot}$ , we would surmise that disks could not have total masses larger than  $\sim 0.1 M_{\odot}$  ( $100 M_J$ ) because disks more massive would become gravitationally unstable.

<sup>5</sup> The detection rate for planets less massive than Neptune, however, seems to rise for lower-mass stars (e.g., Mulders et al. 2015). Since more massive planets put more demanding constraints on initial disk masses, we focus on the statistics of massive, Jupiter-like planets in this paper.

Figure 5 suggests that adjusting the distribution up substantially, to account for uncertain opacity, is not physically plausible if the gas-to-dust ratio is 100, since it would produce some disks with more than  $100 M_J$  of material. However if the gas-to-dust ratio is only 10, then such an adjustment is allowed on physical grounds. Such an adjustment might also produce many systems with sufficient solids to form giant planet cores within gas disk lifetimes.

## 5. CONCLUSIONS

We presented ALMA observations of compact emission from protoplanetary disks in the OMC1 outflow region of the Orion Nebula. We mosaicked a field containing  $\sim 600$  near-IR-identified young stars, of which approximately 100 are known proplyds identified with HST. We detected continuum emission at 1 mm wavelengths towards  $\sim 20\%$  of the proplyd sample, and  $\sim 8\%$  of the larger sample of near-IR objects.

Using standard assumptions about the dust opacities and gas-to-dust ratios, we converted our measured fluxes into dust and dust+gas disk masses. The  $4\sigma$  detection threshold in our map corresponds to a (dust+gas) disk mass of  $\sim 1.5 M_J$ . The fraction of disks with more than  $10 M_J$  is  $\sim 2\%$ , similar to the detection rate of planets around M dwarfs; M dwarfs are the dominant stellar constituent of the ONC.

None of the sources detected in continuum emission are seen in CO(2-1) or C<sup>18</sup>O(2-1) emission. While computing the emission in a single transition is highly uncertain, even the full range of existing models predicts that disks with gas-to-dust ratio of 100 would be detected in our observations. Since none were, we suggest that disks in this region have gas-to-dust ratios that are substantially lower than 100.

The disks detected here, which appear to be gas poor, still have substantial solid content. With a standard dust opacity assumption, our measurements suggest that 2% of disks have enough solids to build Jupiter-mass cores. However solids may already be sequestered in larger bodies at the age of our sample, in which case our measurements would be consistent with higher solid disk masses. Such disks are physically plausible, because the low gas-to-dust ratio means that high solid masses need not lead to global gravitational instability. Since uncertain opacities allow inferred dust disk masses to be adjusted upwards, the potential for giant planet formation likely exists around significantly more than 2% of ONC cluster members.

This work was supported by NSF AAG grant 1311910. The National Radio Astronomy Observatory is a facility of the National Science Foundation operated under cooperative agreement by Associated Universities, Inc. The results reported herein benefitted from collaborations and/or information exchange within NASA’s Nexus for Exoplanet System Science (NExSS) research coordination network sponsored by NASA’s Science Mission Directorate.

## REFERENCES

- Alibert, Y., Mordasini, C., Benz, W., & Winisdoerffer, C. 2005, *A&A*, 434, 343
- Andrews, S. M., Rosenfeld, K. A., Kraus, A. L., & Wilner, D. J. 2013, *ApJ*, 771, 129
- Andrews, S. M. & Williams, J. P. 2005, *ApJ*, 631, 1134
- . 2007, *ApJ*, 671, 1800
- Ansdell, M., Williams, J. P., & Cieza, L. A. 2015, *ApJ*, 806, 221
- Bally, J., Ginsburg, A., Silvia, D., & Youngblood, A. 2015a, *A&A*, 579, A130
- Bally, J., Mann, R. K., Eisner, J. A., et al. 2015b, *ApJ*, 808, 69
- Bally, J., Testi, L., Sargent, A., & Carlstrom, J. 1998, *AJ*, 116, 854
- Beckwith, S. V. W., Sargent, A. I., Chini, R. S., & Guesten, R. 1990, *AJ*, 99, 924
- Carpenter, J. M. 2000, *AJ*, 120, 3139
- . 2002, *AJ*, 124, 1593
- Carpenter, J. M., Ricci, L., & Isella, A. 2014, *ApJ*, 787, 42
- Cieza, L., Williams, J., Kourkchi, E., et al. 2015, *MNRAS*, 454, 1909
- Cumming, A., Butler, R. P., Marcy, G. W., et al. 2008, *PASP*, 120, 531
- D’Antona, F. & Mazzitelli, I. 1994, *ApJS*, 90, 467
- Desch, S. J. 2007, *ApJ*, 671, 878
- Eisner, J. A. & Carpenter, J. M. 2003, *ApJ*, 598, 1341
- . 2006, *ApJ*, 641, 1162
- Eisner, J. A., Plambeck, R. L., Carpenter, J. M., et al. 2008, *ApJ*, 683, 304
- Felli, M., Churchwell, E., Wilson, T. L., & Taylor, G. B. 1993a, *A&AS*, 98, 137
- Felli, M., Taylor, G. B., Catarzi, M., Churchwell, E., & Kurtz, S. 1993b, *A&AS*, 101, 127
- Forbrich, J., Preibisch, T., Menten, K. M., et al. 2007, *A&A*, 464, 1003
- Hayashi, C. 1981, *Progress of Theoretical Physics*, 70, 35
- Hester, J. J. & Desch, S. J. 2005, in *Astronomical Society of the Pacific Conference Series*, Vol. 341, *Chondrites and the Protoplanetary Disk*, ed. A. N. Krot, E. R. D. Scott, & B. Reipurth, 107
- Hildebrand, R. H. 1983, *QJRAS*, 24, 267
- Hillenbrand, L. A. 1997, *AJ*, 113, 1733
- Hillenbrand, L. A. & Carpenter, J. M. 2000, *ApJ*, 540, 236
- Hillenbrand, L. A., Hoffer, A. S., & Herczeg, G. J. 2013, *AJ*, 146, 85
- Hillenbrand, L. A., Strom, S. E., Calvet, N., et al. 1998, *AJ*, 116, 1816
- Ingraham, P., Albert, L., Doyon, R., & Artigau, E. 2014, *ApJ*, 782, 8
- Johnson, J. A., Aller, K. M., Howard, A. W., & Crepp, J. R. 2010, *PASP*, 122, 905
- Johnstone, D., Hollenbach, D., & Bally, J. 1998, *ApJ*, 499, 758
- Kraus, S., Balega, Y. Y., Berger, J.-P., et al. 2007, *A&A*, 466, 649
- Lada, C. J., Depoy, D. L., Merrill, K. M., & Gatley, I. 1991, *ApJ*, 374, 533
- Lada, C. J. & Lada, E. A. 2003, *ARA&A*, 41, 57
- Lada, C. J., Muench, A. A., Haisch, K. E., et al. 2000, *AJ*, 120, 3162
- Lada, E. A., Strom, K. M., & Myers, P. C. 1993, in *Protostars and Planets III*, 245–277
- Luhman, K. L., Rieke, G. H., Young, E. T., et al. 2000, *ApJ*, 540, 1016
- Mann, R. K., Andrews, S. M., Eisner, J. A., et al. 2015, *ApJ*, 802, 77
- Mann, R. K., Di Francesco, J., Johnstone, D., et al. 2014, *ApJ*, 784, 82
- Mann, R. K. & Williams, J. P. 2009, *ApJ*, 694, L36
- . 2010, *ApJ*, 725, 430
- Menten, K. M., Reid, M. J., Forbrich, J., & Brunthaler, A. 2007, *A&A*, 474, 515
- Miotello, A., Bruderer, S., & van Dishoeck, E. F. 2014, *A&A*, 572, A96
- Mulders, G. D., Pascucci, I., & Apai, D. 2015, *ApJ*, 814, 130
- Mundy, L. G., Looney, L. W., & Lada, E. A. 1995, *ApJ*, 452, L137
- Pollack, J. B., Hubickyj, O., Bodenheimer, P., et al. 1996, *Icarus*, 124, 62
- Prosser, C. F., Stauffer, J. R., Hartmann, L., et al. 1994, *ApJ*, 421, 517
- Ricci, L., Robberto, M., & Soderblom, D. R. 2008, *AJ*, 136, 2136
- Richert, A. J. W., Feigelson, E. D., Getman, K. V., & Kuhn, M. A. 2015, *ApJ*, 811, 10
- Sandstrom, K. M., Peek, J. E. G., Bower, G. C., Bolatto, A. D., & Plambeck, R. L. 2007, *ApJ*, 667, 1161
- Sclally, A. & Clarke, C. 2001, *MNRAS*, 325, 449
- Sheehan, P. D., Eisner, J. A., Mann, R. K., & Williams, J. P. 2016, *ApJ*, submitted
- Slesnick, C. L., Hillenbrand, L. A., & Carpenter, J. M. 2004, *ApJ*, 610, 1045
- Snell, R. L., Scoville, N. Z., Sanders, D. B., & Erickson, N. R. 1984, *ApJ*, 284, 176
- Throop, H. B. & Bally, J. 2005, *ApJ*, 623, L149
- Tobin, J. J., Hartmann, L., Furesz, G., Mateo, M., & Megeath, S. T. 2009, *ApJ*, 697, 1103
- Vicente, S. M. & Alves, J. 2005, *A&A*, 441, 195
- Weidenschilling, S. J. 1977, *Ap&SS*, 51, 153
- Williams, J. P., Andrews, S. M., & Wilner, D. J. 2005, *ApJ*, 634, 495
- Williams, J. P. & Best, W. M. J. 2014, *ApJ*, 788, 59
- Williams, J. P., Cieza, L. A., Andrews, S. M., et al. 2013, *MNRAS*, 435, 1671
- Williams, J. P. & Gaidos, E. 2007, *ApJ*, 663, L33
- Williams, J. P., Mann, R. K., Di Francesco, J., et al. 2014, *ApJ*, 796, 120
- Wright, J. T., Fakhouri, O., Marcy, G. W., et al. 2011, *PASP*, 123, 412
- Zapata, L. A., Rodríguez, L. F., Kurtz, S. E., O’Dell, C. R., & Ho, P. T. P. 2004, *ApJ*, 610, L121

TABLE 3  
FLUXES OBSERVED TOWARD NON-DETECTED SOURCE POSITIONS

ID	$\alpha$ (J2000)	$\delta$ (J2000)	$F_{\lambda 1.3\text{mm}}$ (mJy)	Local Noise (mJy)	S/N
HC634	5 35 8.43	-5 21 19.80	0.4	0.2	2.0
HC382	5 35 8.74	-5 22 56.70	0.7	0.4	1.9
HC674	5 35 9.49	-5 20 58.80	0.0	0.4	0.0
HC579	5 35 9.53	-5 21 48.10	0.2	0.2	0.7
HC748	5 35 9.70	-5 21 52.10	0.3	0.3	1.2
HC627	5 35 9.70	-5 21 24.90	0.7	0.2	3.4
HC621	5 35 9.78	-5 21 28.30	0.2	0.2	1.0
HC630	5 35 9.90	-5 21 22.50	0.1	0.2	0.5
HC671	5 35 10.20	-5 21 0.40	0.3	0.3	1.2
HC553	5 35 10.27	-5 21 57.20	0.4	1.3	0.3
HC605	5 35 10.43	-5 21 34.60	0.2	0.2	1.1
HC466	5 35 10.45	-5 22 27.30	0.2	0.7	0.3
HC612	5 35 10.47	-5 21 32.50	0.4	0.2	1.9
HC570	5 35 10.47	-5 21 49.60	0.1	0.4	0.2
HC417	5 35 10.49	-5 22 45.80	0.4	0.3	1.2
HC810	5 35 10.50	-5 20 21.03	0.0	0.4	0.1
HC500	5 35 10.54	-5 22 16.60	-0.8	0.6	-1.3
HC789	5 35 10.58	-5 21 14.08	1.3	1.3	1.0
HC385	5 35 10.62	-5 22 56.10	1.4	1.1	1.4
HC363	5 35 10.65	-5 23 3.40	1.1	1.1	1.0
HC489	5 35 10.71	-5 22 20.30	-0.1	0.9	-0.2
HC392	5 35 10.73	-5 22 54.50	0.5	0.6	0.8
HC576	5 35 10.82	-5 21 48.90	2.1	0.7	3.0
HC426	5 35 10.85	-5 22 40.80	-0.3	0.4	-0.7
HC529	5 35 10.88	-5 22 6.00	-0.1	0.4	-0.2
HC416	5 35 10.90	-5 22 46.40	2.7	0.9	2.9
HC814	5 35 10.98	-5 20 12.94	-0.0	0.1	-0.0
HC473	5 35 10.99	-5 22 24.80	-0.8	0.7	-1.0
HC434	5 35 11.20	-5 22 37.80	0.9	0.5	1.7
HC515	5 35 11.21	-5 22 10.80	-0.0	0.3	-0.1
HC666	5 35 11.29	-5 21 3.10	0.1	0.2	0.4
HC643	5 35 11.32	-5 21 15.60	0.4	0.2	2.4
HC559	5 35 11.37	-5 21 54.00	0.4	0.4	0.9
HC656	5 35 11.51	-5 21 6.40	0.4	0.2	2.1
HC404	5 35 11.63	-5 22 51.70	0.7	0.8	0.9
HC709	5 35 11.63	-5 22 46.10	-0.4	0.6	-0.6
HC539	5 35 11.72	-5 22 3.10	1.2	0.7	1.8
HC555	5 35 11.79	-5 21 55.60	0.6	0.7	0.8
HC794	5 35 11.87	-5 20 43.51	0.4	0.2	2.6
HC818	5 35 11.90	-5 20 2.42	0.1	0.1	0.9
HC664	5 35 11.90	-5 21 3.40	1.0	0.8	1.3
HC708	5 35 11.92	-5 22 50.90	0.6	0.9	0.7
HC569	5 35 11.93	-5 21 50.10	1.4	0.8	1.7
HC536	5 35 11.94	-5 22 4.10	0.7	1.0	0.7
HC772	5 35 11.98	-5 22 8.00	1.4	1.0	1.4
HC395	5 35 11.98	-5 22 54.20	0.8	1.2	0.7
HC803	5 35 12.00	-5 20 33.40	-0.1	0.1	-0.9
HC790	5 35 12.08	-5 21 12.95	0.1	0.3	0.3
HC799	5 35 12.11	-5 20 39.95	0.8	0.2	3.4
HC746	5 35 12.14	-5 21 48.50	-0.6	0.7	-0.9
HC747	5 35 12.16	-5 21 53.80	-1.3	0.7	-1.9
HC751	5 35 12.20	-5 22 30.80	0.2	1.3	0.1
HC808	5 35 12.23	-5 20 26.52	-0.0	0.1	-0.4
HC752	5 35 12.27	-5 22 27.10	-0.8	1.7	-0.5
HC698	5 35 12.28	-5 20 45.20	0.5	0.2	2.7
HC785	5 35 12.31	-5 22 34.19	1.1	1.6	0.7
HC781	5 35 12.35	-5 22 41.35	1.9	1.8	1.1
HC762	5 35 12.37	-5 21 54.80	-0.8	1.2	-0.6
HC692	5 35 12.40	-5 20 47.90	-0.0	0.2	-0.2
HC753	5 35 12.43	-5 22 8.70	-1.6	1.8	-0.9
HC761	5 35 12.46	-5 21 37.80	0.5	1.3	0.4
HC368	5 35 12.58	-5 23 2.00	-2.1	5.0	-0.4
HC795	5 35 12.62	-5 20 43.07	-0.3	0.2	-1.1
HC696	5 35 12.65	-5 20 47.30	-0.2	0.3	-0.8
HC609	5 35 12.67	-5 21 33.40	1.1	1.4	0.8
HC770	5 35 12.68	-5 21 47.60	3.6	1.5	2.4
HC712	5 35 12.77	-5 21 58.90	4.3	1.6	2.7
HC706	5 35 12.79	-5 21 57.90	4.0	1.6	2.5
HC801	5 35 12.81	-5 20 39.16	0.0	0.4	0.1
HC699	5 35 12.83	-5 20 43.60	-0.0	0.3	-0.1
HC659	5 35 12.86	-5 21 5.00	0.3	0.4	0.8
HC780	5 35 12.95	-5 22 44.34	1.6	6.0	0.3
HC683	5 35 13.02	-5 20 52.90	0.2	0.4	0.5
HC544	5 35 13.03	-5 22 1.00	1.1	2.0	0.6
HC505	5 35 13.05	-5 22 15.20	4.3	5.4	0.8

TABLE 3 — *Continued*

ID	$\alpha$ (J2000)	$\delta$ (J2000)	$F_{\lambda 1.3\text{mm}}$ (mJy)	Local Noise (mJy)	S/N
HC562	5 35 13.06	-5 21 53.20	4.4	1.9	2.3
HC599	5 35 13.07	-5 21 39.00	0.8	1.3	0.6
HC805	5 35 13.07	-5 20 30.42	0.1	0.3	0.4
HC402	5 35 13.09	-5 22 53.20	27.2	8.9	3.1
HC707	5 35 13.11	-5 22 47.10	11.9	6.2	1.9
HC648	5 35 13.11	-5 21 13.40	0.8	0.4	1.9
HC487	5 35 13.18	-5 22 21.20	18.5	6.3	2.9
HC523	5 35 13.25	-5 22 9.90	0.5	2.8	0.2
HC380	5 35 13.29	-5 22 57.90	-1.8	9.2	-0.2
HC783	5 35 13.30	-5 22 39.32	3.3	10.8	0.3
HC811	5 35 13.33	-5 20 19.09	0.9	0.4	2.5
HC572	5 35 13.33	-5 21 49.90	-2.1	1.3	-1.6
HC471	5 35 13.37	-5 22 26.20	5.2	11.1	0.5
HC685	5 35 13.38	-5 20 51.60	0.4	0.4	0.9
HC653	5 35 13.44	-5 21 7.40	0.1	0.3	0.2
135-220	5 35 13.51	-5 22 19.49	15.4	8.7	1.8
HC360	5 35 13.53	-5 23 4.50	-7.7	8.5	-0.9
HC788	5 35 13.57	-5 22 9.65	6.3	5.3	1.2
HC800	5 35 13.60	-5 20 39.30	0.8	0.3	2.3
HC804	5 35 13.61	-5 20 31.51	0.5	0.4	1.2
HC633	5 35 13.62	-5 21 21.10	-0.1	0.4	-0.3
HC791	5 35 13.62	-5 21 5.22	-0.2	0.3	-0.5
HC483	5 35 13.75	-5 22 22.00	11.2	21.0	0.5
HC499	5 35 13.78	-5 22 17.40	8.2	14.0	0.6
HC541	5 35 13.81	-5 22 2.80	17.6	4.8	3.7
HC548	5 35 13.81	-5 21 59.60	-0.5	4.9	-0.1
HC525	5 35 13.83	-5 22 9.10	6.6	7.8	0.9
HC451	5 35 13.97	-5 22 31.90	-13.5	72.0	-0.2
HC629	5 35 13.98	-5 21 23.30	0.9	0.4	2.3
HC552	5 35 13.98	-5 21 58.00	5.7	4.5	1.3
HC760	5 35 14.01	-5 21 51.90	6.3	3.4	1.8
HC704	5 35 14.06	-5 22 5.70	3.4	5.3	0.7
HC705	5 35 14.09	-5 22 23.00	118.7	41.9	2.8
HC438	5 35 14.09	-5 22 36.60	252.2	75.7	3.3
HC779	5 35 14.12	-5 22 22.77	142.8	40.4	3.5
142-301	5 35 14.15	-5 23 0.91	30.3	10.7	2.8
HC815	5 35 14.17	-5 20 8.17	0.5	0.5	1.1
HC809	5 35 14.17	-5 20 23.65	0.5	0.4	1.5
HC787	5 35 14.20	-5 22 12.99	19.1	10.9	1.8
HC690	5 35 14.28	-5 20 48.50	0.5	0.3	1.5
HC361	5 35 14.29	-5 23 4.30	18.9	11.2	1.7
HC458	5 35 14.31	-5 22 30.70	224.8	179.8	1.3
HC537	5 35 14.31	-5 22 4.40	16.3	11.1	1.5
HC345	5 35 14.32	-5 23 8.30	0.0	1.8	0.0
HC448	5 35 14.36	-5 22 32.80	46.4	140.1	0.3
HC399	5 35 14.37	-5 22 54.10	28.5	8.9	3.2
HC439	5 35 14.37	-5 22 36.10	123.5	151.6	0.8
HC391	5 35 14.39	-5 22 55.70	15.0	7.9	1.9
HC300	5 35 14.40	-5 23 23.10	0.9	2.6	0.4
HC784	5 35 14.50	-5 22 38.78	-30.0	46.5	-0.6
HC759	5 35 14.50	-5 22 29.40	169.6	143.8	1.2
HC530	5 35 14.53	-5 22 6.60	-6.5	13.2	-0.5
HC364	5 35 14.54	-5 23 3.70	0.4	1.8	0.2
146-201	5 35 14.61	-5 22 0.94	-12.7	11.4	-1.1
HC545	5 35 14.63	-5 22 1.00	-9.0	12.0	-0.7
HC796	5 35 14.65	-5 20 42.70	-0.1	0.7	-0.2
HC443	5 35 14.66	-5 22 33.80	55.3	138.7	0.4
HC276	5 35 14.66	-5 23 28.70	-1.3	2.0	-0.6
HC369	5 35 14.67	-5 23 1.90	-12.7	6.4	-2.0
HC756	5 35 14.67	-5 22 38.60	34.4	49.1	0.7
HC757	5 35 14.69	-5 22 38.20	-18.3	78.9	-0.2
HC575	5 35 14.69	-5 21 49.50	-1.6	3.7	-0.4
HC411	5 35 14.70	-5 22 49.40	15.5	8.9	1.7
HC812	5 35 14.70	-5 20 17.13	0.8	0.3	2.3
HC755	5 35 14.71	-5 22 35.50	29.1	131.2	0.2
HC302	5 35 14.72	-5 23 22.90	9.1	2.9	3.1
HC465	5 35 14.73	-5 22 29.80	101.2	139.9	0.7
148-305	5 35 14.80	-5 23 4.76	-0.6	7.0	-0.1
HC773	5 35 14.82	-5 22 23.20	-1.5	50.4	-0.0
HC324	5 35 14.84	-5 23 16.00	0.9	2.2	0.4
HC819	5 35 14.84	-5 20 2.29	-0.1	0.4	-0.3
HC771	5 35 14.86	-5 22 44.10	-1.4	11.1	-0.1
HC453	5 35 14.87	-5 22 31.70	-12.8	150.5	-0.1
HC714	5 35 14.88	-5 23 5.10	-1.0	1.9	-0.5
149-329	5 35 14.92	-5 23 29.05	0.3	1.9	0.1
HC431	5 35 14.92	-5 22 39.10	-12.1	22.8	-0.5



TABLE 3 — *Continued*

ID	$\alpha$ (J2000)	$\delta$ (J2000)	$F_{\lambda 1.3\text{mm}}$ (mJy)	Local Noise (mJy)	S/N
HC673	5 35 14.96	-5 21 0.80	0.6	1.5	0.4
150-147	5 35 15.00	-5 21 47.34	13.6	5.5	2.5
HC546	5 35 15.00	-5 22 0.00	4.3	46.4	0.1
HC334	5 35 15.00	-5 23 14.30	2.2	1.6	1.4
HC684	5 35 15.02	-5 20 52.60	1.0	0.6	1.8
HC581	5 35 15.02	-5 21 47.40	14.3	5.5	2.6
150-231	5 35 15.02	-5 22 31.11	-26.6	26.1	-1.0
HC456	5 35 15.04	-5 22 31.20	8.0	22.4	0.4
HC373	5 35 15.04	-5 23 1.10	3.4	2.0	1.7
HC298	5 35 15.07	-5 23 23.40	-1.8	1.8	-1.0
HC694	5 35 15.17	-5 20 48.20	0.4	1.3	0.3
HC359	5 35 15.18	-5 23 5.00	5.8	3.9	1.5
HC813	5 35 15.19	-5 20 15.01	0.0	0.7	0.0
152-319	5 35 15.20	-5 23 18.81	2.8	1.6	1.7
HC687	5 35 15.20	-5 20 51.40	-0.4	1.0	-0.4
HC398	5 35 15.20	-5 22 54.40	-1.1	1.8	-0.6
HC478	5 35 15.21	-5 22 24.10	10.3	9.2	1.1
HC437	5 35 15.21	-5 22 36.70	7.3	8.1	0.9
HC806	5 35 15.27	-5 20 28.99	1.0	1.0	1.0
HC386	5 35 15.27	-5 22 56.70	2.6	1.5	1.7
HC558	5 35 15.27	-5 21 55.70	12.5	11.1	1.1
HC299	5 35 15.30	-5 23 23.20	-0.1	1.3	-0.1
HC624	5 35 15.30	-5 21 28.80	2.4	2.1	1.1
HC739	5 35 15.32	-5 20 55.00	-0.8	0.9	-0.8
154-324	5 35 15.35	-5 23 24.11	-0.2	1.3	-0.2
HC476	5 35 15.35	-5 22 25.20	8.0	6.2	1.3
HC310	5 35 15.35	-5 23 21.40	1.4	1.5	0.9
HC504	5 35 15.35	-5 22 15.60	-3.4	12.3	-0.3
HC792	5 35 15.37	-5 20 47.37	-1.3	1.4	-0.9
154-225	5 35 15.37	-5 22 25.35	8.0	5.8	1.4
154-240	5 35 15.38	-5 22 39.85	25.7	14.1	1.8
HC600	5 35 15.41	-5 21 39.50	4.4	2.4	1.8
HC646	5 35 15.41	-5 21 14.00	1.3	1.9	0.6
HC413	5 35 15.49	-5 22 48.60	4.2	2.5	1.7
HC327	5 35 15.54	-5 23 15.80	0.7	1.3	0.5
HC419	5 35 15.55	-5 22 46.40	9.4	11.6	0.8
HC274	5 35 15.56	-5 23 29.60	3.0	2.7	1.1
HC786	5 35 15.56	-5 22 20.13	17.5	21.8	0.8
HC378	5 35 15.60	-5 22 58.90	4.4	4.7	0.9
HC389	5 35 15.64	-5 22 56.40	2.9	4.7	0.6
157-323	5 35 15.72	-5 23 22.59	2.5	2.8	0.9
HC344	5 35 15.77	-5 23 9.90	2.2	1.2	1.8
HC598	5 35 15.77	-5 21 39.80	2.2	2.2	1.0
HC336	5 35 15.81	-5 23 14.30	0.4	1.3	0.3
158-326	5 35 15.81	-5 23 25.51	10.7	2.9	3.7
HC340	5 35 15.81	-5 23 12.00	1.7	1.2	1.4
HC291	5 35 15.84	-5 23 25.60	10.7	2.8	3.8
HC420	5 35 15.84	-5 22 45.90	3.0	2.8	1.1
HC447	5 35 15.89	-5 22 33.20	4.6	3.2	1.4
159-221	5 35 15.93	-5 22 21.05	9.4	4.1	2.3
HC490	5 35 15.95	-5 22 21.10	9.6	4.2	2.3
HC769	5 35 15.96	-5 22 41.10	6.2	3.3	1.9
HC304	5 35 15.97	-5 23 22.70	0.9	2.8	0.3
HC565	5 35 16.01	-5 21 53.10	-1.9	11.7	-0.2
161-324	5 35 16.05	-5 23 24.35	3.5	2.9	1.2
HC350	5 35 16.06	-5 23 7.30	4.6	1.2	3.9
HC296	5 35 16.07	-5 23 24.30	3.5	2.8	1.2
161-328	5 35 16.07	-5 23 27.81	3.4	2.7	1.3
HC401	5 35 16.08	-5 22 54.10	-1.5	1.3	-1.2
161-314	5 35 16.10	-5 23 14.05	1.1	1.8	0.6
HC303	5 35 16.10	-5 23 23.20	-0.3	2.7	-0.1
HC354	5 35 16.11	-5 23 6.80	4.7	1.2	4.0
HC511	5 35 16.12	-5 22 12.50	-4.1	5.3	-0.8
HC393	5 35 16.14	-5 22 55.20	-0.1	1.2	-0.0
HC768	5 35 16.14	-5 22 45.10	-0.2	2.4	-0.1
HC520	5 35 16.18	-5 22 11.30	0.4	5.0	0.1
HC435	5 35 16.20	-5 22 37.50	-3.7	2.8	-1.3
HC758	5 35 16.24	-5 22 24.30	3.5	2.2	1.6
HC317	5 35 16.24	-5 23 19.10	-0.3	1.8	-0.1
163-210	5 35 16.27	-5 22 10.45	2.2	4.2	0.5
HC522	5 35 16.29	-5 22 10.40	2.2	4.1	0.5
163-222	5 35 16.30	-5 22 21.50	3.0	2.1	1.4
HC479	5 35 16.31	-5 22 24.00	1.4	2.0	0.7
HC488	5 35 16.32	-5 22 21.60	3.0	2.1	1.4
163-249	5 35 16.33	-5 22 49.01	-1.3	1.5	-0.9
HC292	5 35 16.35	-5 23 25.30	-0.2	1.8	-0.1

TABLE 3 — *Continued*

ID	$\alpha$ (J2000)	$\delta$ (J2000)	$F_{\lambda 1.3\text{mm}}$ (mJy)	Local Noise (mJy)	S/N
HC485	5 35 16.38	-5 22 22.30	-0.8	1.9	-0.4
HC341	5 35 16.41	-5 23 11.50	1.1	2.0	0.5
HC514	5 35 16.43	-5 22 12.20	6.7	2.7	2.4
HC309	5 35 16.46	-5 23 23.00	-1.3	1.6	-0.8
165-235	5 35 16.48	-5 22 35.16	-0.3	1.5	-0.2
HC390	5 35 16.49	-5 22 56.50	1.4	1.1	1.3
HC442	5 35 16.50	-5 22 35.20	-0.3	1.5	-0.2
165-254	5 35 16.54	-5 22 53.70	-0.1	1.2	-0.1
166-250	5 35 16.59	-5 22 50.36	-0.1	1.5	-0.0
166-316	5 35 16.61	-5 23 16.19	1.8	2.5	0.7
HC325	5 35 16.63	-5 23 16.10	3.6	2.4	1.5
HC567	5 35 16.65	-5 21 52.70	-0.4	5.1	-0.1
HC280	5 35 16.66	-5 23 28.90	-0.5	2.8	-0.2
HC293	5 35 16.73	-5 23 25.20	-0.2	2.3	-0.1
167-231	5 35 16.73	-5 22 31.30	3.0	1.6	1.9
168-328	5 35 16.77	-5 23 28.06	5.5	2.8	2.0
HC518	5 35 16.78	-5 22 11.70	-1.3	2.1	-0.6
168-235	5 35 16.81	-5 22 34.71	0.6	1.3	0.5
HC349	5 35 16.87	-5 23 7.10	0.4	0.7	0.5
HC484	5 35 16.90	-5 22 22.50	-1.0	1.5	-0.7
HC441	5 35 16.91	-5 22 35.20	0.6	1.3	0.4
HC397	5 35 16.91	-5 22 55.10	1.7	0.8	2.2
HC494	5 35 16.94	-5 22 20.70	-1.0	1.4	-0.7
HC524	5 35 16.94	-5 22 9.90	-1.6	1.4	-1.2
HC450	5 35 17.01	-5 22 33.10	-0.2	1.5	-0.1
HC410	5 35 17.12	-5 22 50.10	0.5	1.3	0.4
HC517	5 35 17.13	-5 22 11.90	-2.2	1.3	-1.7
HC315	5 35 17.16	-5 23 20.40	1.6	1.3	1.3
HC330	5 35 17.24	-5 23 16.60	-0.2	1.1	-0.2
HC493	5 35 17.34	-5 22 21.20	1.0	0.8	1.2
174-305	5 35 17.37	-5 23 4.86	0.7	0.5	1.3
HC540	5 35 17.40	-5 22 3.70	0.5	1.0	0.5
HC313	5 35 17.47	-5 23 21.10	1.8	1.3	1.4
176-325	5 35 17.55	-5 23 24.96	4.0	1.6	2.5
HC550	5 35 17.55	-5 22 0.30	0.5	1.1	0.4
HC388	5 35 17.56	-5 22 56.80	1.6	0.7	2.3
HC295	5 35 17.57	-5 23 24.90	4.0	1.6	2.5
HC469	5 35 17.58	-5 22 27.80	0.4	0.6	0.7
HC513	5 35 17.62	-5 22 12.60	2.2	0.7	3.4
HC563	5 35 17.62	-5 21 53.90	1.7	2.0	0.9
176-252	5 35 17.64	-5 22 51.66	0.3	0.7	0.4
HC527	5 35 17.66	-5 22 7.90	0.8	0.6	1.2
HC405	5 35 17.66	-5 22 51.70	0.6	0.7	0.9
HC333	5 35 17.74	-5 23 14.90	1.5	1.0	1.5
HC462	5 35 17.76	-5 22 31.00	1.8	0.6	3.0
HC332	5 35 17.82	-5 23 15.60	3.0	1.0	3.0
HC496	5 35 17.83	-5 22 19.60	-0.2	0.8	-0.2
HC367	5 35 17.87	-5 23 3.10	0.4	0.6	0.7
HC542	5 35 17.88	-5 22 3.00	-0.5	0.8	-0.6
HC425	5 35 17.95	-5 22 45.50	1.1	0.6	1.8
HC501	5 35 18.03	-5 22 18.20	2.6	0.8	3.4
HC535	5 35 18.03	-5 22 5.50	-0.6	0.6	-1.0
180-331	5 35 18.03	-5 23 30.80	4.2	1.2	3.5
HC271	5 35 18.05	-5 23 30.80	4.2	1.2	3.6
HC372	5 35 18.08	-5 23 1.80	0.3	0.6	0.5
182-316	5 35 18.19	-5 23 31.55	0.2	1.0	0.2
HC533	5 35 18.24	-5 22 6.30	0.4	0.4	0.9
HC331	5 35 18.25	-5 23 15.70	2.3	0.8	2.7
HC348	5 35 18.28	-5 23 7.50	0.3	0.4	0.8
HC430	5 35 18.40	-5 22 40.00	0.6	0.5	1.1
HC278	5 35 18.50	-5 23 29.30	0.2	0.9	0.2
HC384	5 35 18.53	-5 22 58.10	0.6	0.4	1.5
HC463	5 35 18.58	-5 22 31.00	1.1	0.5	2.4
HC337	5 35 18.67	-5 23 14.00	1.2	0.8	1.5
HC713	5 35 18.71	-5 22 56.90	1.0	0.4	2.6
HC543	5 35 18.76	-5 22 2.20	0.4	0.4	0.8
189-329	5 35 18.87	-5 23 28.85	2.6	0.9	2.8
HC352	5 35 18.88	-5 23 7.20	0.6	0.6	1.0
HC498	5 35 18.96	-5 22 18.80	0.3	0.8	0.4
HC311	5 35 18.97	-5 23 22.00	0.0	0.7	0.0
190-251	5 35 19.03	-5 22 50.65	1.0	0.4	2.4
HC357	5 35 19.11	-5 23 6.30	-0.4	0.6	-0.7
HC288	5 35 19.12	-5 23 27.10	1.4	0.8	1.8
HC444	5 35 19.14	-5 22 34.60	-0.1	0.4	-0.2
HC408	5 35 19.22	-5 22 50.70	-0.2	0.4	-0.6
HC356	5 35 19.38	-5 23 6.50	0.6	0.6	1.0

TABLE 3 — *Continued*

ID	$\alpha$ (J2000)			$\delta$ (J2000)			$F_{\lambda 1.3\text{mm}}$ (mJy)	Local Noise (mJy)	S/N
HC491	5	35	19.47	-5	22	21.80	1.8	0.6	2.9
HC446	5	35	19.68	-5	22	34.20	0.1	0.3	0.4
HC531	5	35	19.90	-5	22	7.30	-0.7	0.4	-1.8
HC564	5	35	19.97	-5	21	54.00	0.3	0.6	0.6
HC452	5	35	19.98	-5	22	32.80	0.3	0.6	0.5
HC766	5	35	20.00	-5	23	28.80	1.0	0.5	2.2
HC474	5	35	20.03	-5	22	26.50	0.2	0.7	0.3
HC365	5	35	20.13	-5	23	4.50	0.8	0.5	1.6
HC346	5	35	20.18	-5	23	8.50	0.6	0.6	1.0
HC510	5	35	20.40	-5	22	13.70	-0.0	0.5	-0.1